Article

# Compensation between Surface Energy and hcp/fcc Phase Energy of Late Transition Metals from First-Principles Calculations

Hao Lin,[||] Jin-Xun Liu,[||] Hongjun Fan,* and Wei-Xue Li*

Read Online

ACCESS | Metrics & More | Article Recommendations

ABSTRACT: Crystal structures and surface energies of transition metals are of fundamental importance to the activity, selectivity, and stability in heterogeneous catalysis, but the interplay between crystal structures and surface energies as well as its dependence on composition remains elusive. In the present work, we performed comprehensive density functional theory calculations of Co, Ni, Ru, Rh, Pd, Os, and Ir in both hexagonal close-packed (hcp) and face-centered cubic (fcc) phases and considered numerous surfaces to derive the equilibrium morphology and the surface energy. Irrespective of the transition metals considered, the fcc phase exposes mainly {111} and {100} facets, whereas the hcp phase exposes mainly {0001}, {10$\bar{1}$0}, and {10$\bar{1}$1} facets. For Co, Ru, and Os preferring the hcp bulk at ambient conditions, the corresponding surface energies are found higher to be than those in the fcc bulk, whereas for Ni, Rh, Pd, and Ir preferring the fcc bulk phase at ambient conditions, the opposite trend is found. A negative linear relationship of the surface energy difference between the fcc and hcp phases with respect to the corresponding bulk energy difference is established; a phase with a higher bulk energy has a lower surface energy as compensation. The compensation effect on the surface energy and the bulk energy provides a driving force for the size-induced phase transition of the nanoparticles. The results are used to rationalize the available experiments, and the insights revealed might be used to design better catalysts.
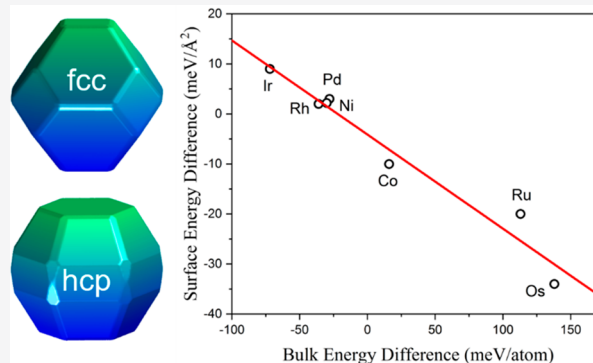
INTRODUCTION

Transition metals (TMs) have been widely used to catalyze various chemical reactions in heterogeneous catalysis.[1,2] Corresponding catalysts with specific size and shape are prepared to expose more coordinate-unsaturated sites and/or unique ensembles (such as B5 sites) to optimize the catalytic activity and selectivity.[3−6] Exploring the sensitivity of active sites with different structural motifs is thus important to design new catalysts.[7−11] Among others, there has been increasing interest in the effect of crystal structures on heterogeneous catalysis and electrocatalysis.[12−14] The great impact of crystal phases on catalysis mainly comes from their distinct bulk symmetries, which might result in various structural motifs with highly different reactivity and density.[15−17] Many experiments reported that for Fischer−Tropsch synthesis (FTS) cobalt with a hexagonal closed-pack (hcp) phase is more active than that with a face-centered cubic (fcc) one.[18−22] Theoretical calculation found that higher activity of hcp Co came from the exposure of more open surfaces with higher intrinsic activity.[23] However, for ruthenium, the fcc phase was able to expose more active sites and therefore have a higher specific activity than hcp Ru, as confirmed by subsequent FTS experiment.[24] Higher activity of fcc Ru than hcp Ru is also found for CO oxidation, hydrogen oxidation

reaction, ammonia−borane, oxygen evolution reaction, hydrogenation reaction, and N_2 activation.[25−32] Additionally, it is also found that CO methanation and aqueous-phase reforming of glycerol over Ni are crystal structure dependent.[33,34] Investigations of different crystal phases of transition metals and their phase transition are therefore helpful to rationalize the involved structure−activity relationship of supported nanocatalysts at relevant catalytic reaction conditions.

For bulk TMs at ambient conditions, the favorable crystal phase follows the sequence of hcp-bcc-hcp-fcc, from the left to right side of the periodic table, due to their different electron configurations.[35] For catalytic relevant bulk metals at ambient conditions, Co, Ru, and Os prefer the hcp phase, whereas the late transition metals such as Ni, Cu, Rh, Pd, Ag, Ir, Pt, and Au prefer the fcc phase.[36−42] At elevated temperatures and high pressures, which are applied typically for most catalytic
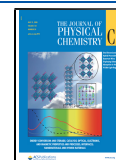
reactions, the active phase of the metal catalysts might transit from one phase to another.[43−45] Since most catalysts are highly dispersed and interact strongly with the substrates underneath,[46,47] the surface/interface effect would become important.[48,49] In particular, when decreasing the particle size to nanometers, the contribution of the surface energy to the overall energetics of a nanoparticle increases dramatically and might change the relative stability of nanoparticles with different phases.[50] However, it is unclear yet how surface energy changes with the crystal phases and the compositions, and what the impact is on the phase transition with respect to the decrease of the particle size.

To shed further light on this, we performed extensive DFT calculations on the surface energies of fcc and hcp TMs including Co, Ni, Ru, Rh, Pd, Os, and Ir. In order to get the overall surface energy, numerous surfaces with different orientations (13 for fcc and 12 for hcp) were considered. The equilibrium morphology of these TMs is derived, and the fcc phase is found to be dominated by {111} and {100} facets, whereas the hcp phase is dominated by {10$\bar{1}$0}, {10$\bar{1}$1}, and {0001} facets, irrespective of the TMs considered. Based on the optimized morphologies, the corresponding overall surface energies are calculated. For Co, Ru, and Os, the corresponding hcp surface energies are found to be higher than those of the fcc phase, whereas for Ni, Rh, Pd, and Ir, the opposite trend is found. A negative linear relationship of the surface energy difference between the fcc and hcp phases with respect to the corresponding bulk energy difference is established. The lower the bulk energy of a crystal phase, the higher the surface energy as compensation. The compensation effect provides a potential driving force for the phase transition for small particles, which might be used to design better catalysts.

METHODOLOGY

All spin-polarized DFT calculations were performed using the Vienna *Ab Initio* Simulation Package (VASP)[51−53] within the projector augmented wave (PAW) approach.[54,55] The exchange-correlation effects were modeled using the Perdew−Burke−Ernzerhof (PBE) generalized gradient approximation (GGA) functional,[56,57] and the plane wave cutoff energy was specified as 400 eV. The energy and maximum force convergence thresholds were set to 10^{-5} eV and 0.01 eV/Å, respectively. The Methfessel−Paxton method was chosen as the smearing algorithm,[58] and the blocked Davidson iteration scheme was chosen as the electron minimization algorithm.[59] Γ-centered k-points meshes of 50/a × 50/b × 50/c and 50/a × 50/b × 1 were used for bulk and slab calculations, respectively. We used vacuum thicknesses of 15 Å to separate the interactions between neighboring slabs to ensure convergence.

Surface free energy is the energy cost to create a new surface per unit area by truncating the metal−metal bond through the specific surface. The accurate measurement of surface energies, especially for high-index facets, remains difficult and even unavailable for the metastable phase.[60] In contrast, DFT provides a systematic method to calculate surface energy.[61−64] In the present work, the surface energy γ_{hkl} of the TMs facet featuring Miller-index (hkl) can be calculated by taking the energy difference between the total energy of an N-layer slab (E_N) and an equivalent bulk reference amount (NE_B) per surface area, determined by

$$\gamma_{hkl} = \lim_{N \to \infty} (E_N - NE_B)/2A \qquad (1)$$

A is the surface area of the slab model. We then use the method suggested by Fiorentini and Methfessel to minimize the possible numerical error introduced by a different supercell.[65] Specifically, for sufficiently large N, varying from 15 to 40, depending on the surface orientation, one can rewrite eq 1 as

$$E_N = 2\gamma_{hkl}A + E_B \times N \qquad (2)$$

Obviously, if the total energy of the slab depends linearly on the slab thickness N, the slope and intercept give the bulk energy and surface energy, respectively.

By using the calculated surface energies, the equilibrium morphology of a freestanding particle can be obtained by the Gibbs−Wulff theorem.[66,67] The Wulff construction can be executed as follows: starting from a center point, a plane that is normal to the $\langle hkl \rangle$ vector (taking fcc as an example) is drawn at the distance of $d_{hkl} = C \times \gamma_{hkl}$, where C is a given constant and γ_{hkl} is the surface energy of unit area normal to the $\langle hkl \rangle$ vector. Once this process is repeated for all the Miller-index planes, the polyhedron that lines inside all the planes gives the equilibrium morphology of the crystal. The Wulff morphologies of various TMs were constructed by VESTA software in the present work.[68] Given that the transition metals expose different facets i with surface energy γ_i and corresponding surface ratio f_i, the overall surface energy γ is calculated via

$$\gamma = \sum_i f_i \times \gamma_i \qquad (3)$$

RESULTS AND DISCUSSION

Bulk Property. We first describe here the calculated bulk properties. For convenience, we classify the TMs considered into two groups based on their favorable bulk structure at ambient conditions: Group **I**, in which Co, Ru, and Os prefer the hcp phase, and Group **II**, in which Ni, Rh, Pd, and Ir prefer the fcc phase. Calculated bulk energy differences per atom between the fcc and hcp phases $(\Delta E_B(\text{fcc} - \text{hcp}))$ and the corresponding optimized lattice constants are shown in Figure 1 and Table 1, respectively. From Figure 1, it can be found that for the TMs in Group **I**, the hcp bulk energies are all lower
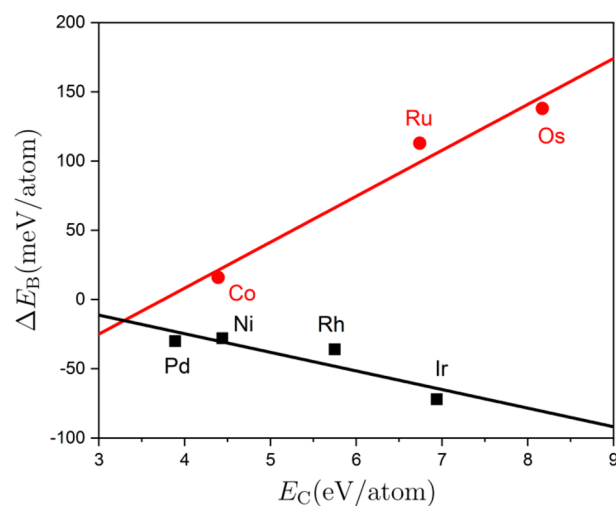

Figure 1. Relationship between crystal phase energy (ΔE_B) and the experimentally measured cohesive energy (E_C) of the seven late transition metals in their most stable bulk phase.

Table 1. Optimized Lattice Constants (*a* for fcc Phase, *a* and *c* for hcp Phase, Å) of Seven Late Transition Metals[a]

	fcc		hcp				
elements	*a*	expt	*a*	expt	*c*	expt	ΔE_B
Co	3.520	3.544[69]	**2.491**	**2.507[70]**	**4.027**	**4.070**	16
Ru	3.818	3.87[76]	**2.727**	**2.706[71]**	**4.300**	**4.282**	113
Os	3.855	3.810[72]	**2.754**	**2.735[72]**	**4.343**	**4.319**	138
Ni	**3.520**	**3.524[77]**	2.482	2.622[79]	4.097	4.321	−28
Rh	**3.841**	**3.804[69]**	2.729	2.78[81]	4.408	4.64	−36
Pd	**3.949**	**3.891[78]**	2.771	2.64[82]	4.653	4.88	−30
Ir	**3.877**	**3.839[78]**	2.751	−	4.464	−	−72

[a]Experimental lattice constants we can obtain so far are also listed. The calculated bulk energy differences between the fcc and hcp phases per atom (ΔE_B, meV/atom) are tabulated in the last column. The lattice constants for the favorable crystal structure of transition metals under ambient conditions are highlighted in bold text.

Table 2. Calculated Surface Energies γ_i of Late Transition Metals with fcc Crystal Structure in Unit of meV/Å², f_i is Corresponding Exposure Surface Ratio (%)[a]

	Co		Ru		Os		Ni		Rh		Pd		Ir	
fcc	γ_i	f_i	γ_i	f_i	γ_i	f_i	γ_i	f_i	γ_i	f_i	γ_i	f_i	γ_i	f_i
{100}	153	14	187	6	227	6	136	20	145	17	94.1	19	175	12
{110}	150	10	173	2	207	−	140	−	148	4	99.4	−	176	−
{111}	129	62	148	61	168	65	119	56	125	65	83.3	51	142	56
{210}	162	−	191	−	235	−	148	−	157	−	102	1	188	−
{211}	152	−	175	4	206	1	137	6	146	−	95.1	4	169	−
{221}	146	−	165	6	191	−	134	−	141	6	93.1	10	162	−
{310}	164	−	191	1	231	−	148	−	156	1	101	2	189	−
{311}	156	9	183	9	223	−	142	1	150	8	100	−	179	−
{320}	159	−	188	−	226	−	146	−	155	−	102	−	184	−
{321}	155	−	178	3	211	−	143	−	152	−	99.1	−	178	−
{322}	144	−	166	−	190	15	131	3	140	−	90.8	10	157	18
{331}	151	−	169	8	197	−	136	12	146	−	96.5	−	170	−
{332}	140	4	161	−	183	14	129	1	138	−	90.2	2	154	14
γ	136		159		179		125		134		87.4		150	

[a]−, exposure ratio less than 1%; γ is the resultant overall surface energy.

Table 3. Calculated Surface Energies γ_i of Late Transition Metals with hcp Crystal Structure in Unit of meV/Å², f_i is Corresponding Exposure Surface Ratio (%)[a]

	Co		Ru		Os		Ni		Rh		Pd		Ir	
hcp	γ_i	f_i	γ_i	f_i	γ_i	f_i	γ_i	f_i	γ_i	f_i	γ_i	f_i	γ_i	f_i
{0001}	131	18	163	15	182	19	115	17	122	17	77.9	18	132	20
{10$\bar{1}$0}	141	24	181	21	213	26	121	23	129	21	84.6	24	142	28
{10$\bar{1}$1}	149	30	180	41	216	40	124	46	130	47	87.2	40	146	47
{10$\bar{1}$2}	156	12	189	13	225	10	135	6	143	4	93.0	9	161	−
{11$\bar{2}$0}	153	7	209	−	256	−	136	1	147	−	95.4	−	174	−
{11$\bar{2}$1}	162	−	204	−	246	−	141	−	149	−	98.0	−	174	−
{11$\bar{2}$2}	161	5	195	5	236	4	137	2	141	7	95.5	4	160	4
{20$\bar{2}$1}	149	3	186	1	222	−	126	1	134	−	89.9	−	153	−
{21$\bar{3}$0}	154	−	205	−	246	−	134	2	143	1	93.8	2	164	−
{21$\bar{3}$1}	160	−	202	2	241	2	139	−	146	−	97.3	−	166	−
{21$\bar{3}$2}	161	1	199	1	241	−	138	1	146	−	97.4	−	166	−
{22$\bar{4}$1}	159	−	207	−	256	−	140	−	144	4	96.2	2	168	−
γ	146		179		213		122		132		85.2		141	

[a]− for exposure ratio less than 1%; γ is the resultant overall surface energy.

than the fcc bulk energies, but the opposite trend is found for the TMs in Group II. This means that for the TMs in Groups I and II, hcp phase and fcc phase is the preferential phase structure, respectively, in perfect agreement with experiments. Specifically, corresponding ΔE_B values are 16, 113, and 138 meV/atom for Co, Ru, and Os, and −28, −36, −30, and −72 meV/atom for Ni, Rh, Pd, and Ir. Moreover, the bulk energy

difference between two phases is proportional to the measured cohesive energy[69] of the favorable crystal phase at ambient conditions. This is understandable, since for a given phase the cohesive energy manifests the binding strength between metal atoms. The larger the cohesive energy, the stronger the binding strength between metal atoms, and so for the energy difference between the two crystal phases.

For lattice constants of the TMs in Group **I**, the optimized *a* and *c* for the hcp phase with a lower bulk energy are all in good agreement with well-documented experiments, and the absolute differences are less than 1.1%.[70−72] Fcc Co, Ru, and Os have been synthesized successfully recently.[25,72−76] Meanwhile, calculated lattice constants of *a* for these TMs of the fcc phase also agree well with experimental measurements, and the absolute differences between them are less than 1.3%. For the TMs in Group **II**, the calculated lattice constants of *a* for the fcc phase with a lower bulk energy are in good agreement with experiment with differences of less than 1.4%.[69,77,78] Compared to Group **I**, hcp phase synthesis for this group metal is difficult, and so far only hcp Ni, Rh, and Pd have been partially reported.[79−82] The absolute differences between calculations and experimental measurements could be as large as ∼5%, possibly due to the poor crystalline state, size effect, and/or presence of ligand, etc.[83]

Surface Energy and Wulff Morphology. Numerous surfaces for both phases, 13 for fcc and 12 for hcp, were considered in the present work, and the calculated surface energies for the TMs considered are given in Table 2 and Table 3, respectively. Based on the calculated individual surface energies, equilibrium morphologies of the fcc and hcp phases via Wulff construction are derived. Figure 2 and Figure
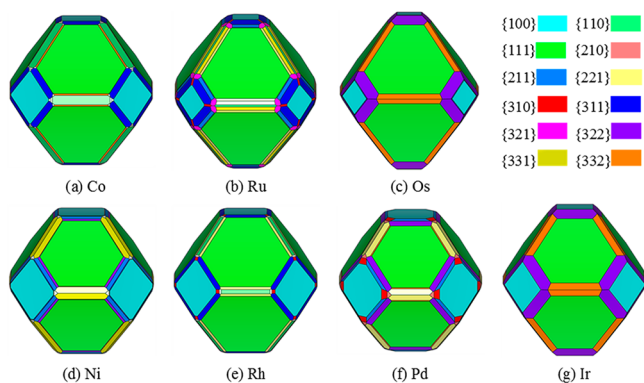

Figure 2. Optimized Wulff morphologies of late transition metals with the fcc crystal structure.

3 present the obtained thermodynamic equilibrium morphologies of the fcc and hcp phases, and the corresponding surface ratios are also given in Table 2 and Table 3, plotted in Figure 4 for better visualization.

For cobalt in Group **I**, we note that the {111} facets have the lowest surface energy of 129 meV/Å² among all fcc Co surfaces
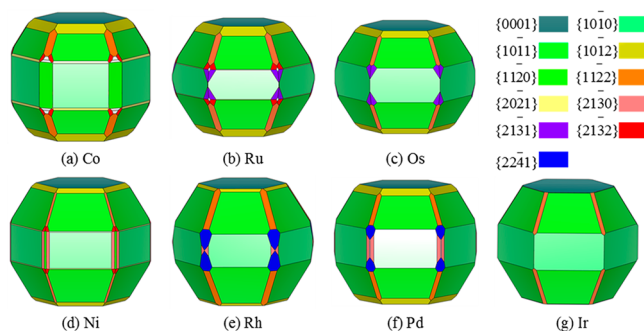

Figure 3. Optimized Wulff morphologies of late transition metals with the hcp crystal structure.
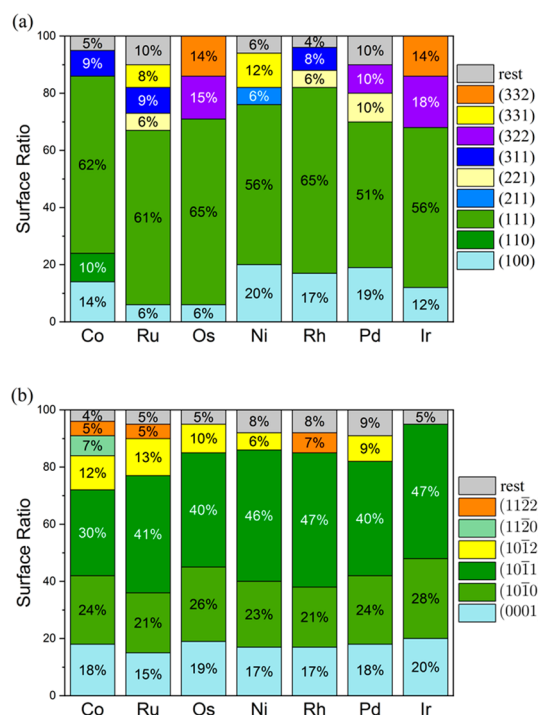

Figure 4. Surface ratio distributions in optimized Wulff morphologies of transition metals with (a) fcc and (b) hcp crystal structures. Those facets with surface ratio less than 5% are included in the "rest".

considered, and the corresponding surface ratio is as high as 62%. The {110}, {100}, and {311} facets have a relatively higher surface energy of 150, 153, and 156 meV/Å², respectively, and the corresponding surface ratios are 10%, 14%, and 9%, respectively. The resulting overall surface energy is 136 meV/Å². For hcp Co, the close-packed {0001} facets have a surface energy of 131 meV/Å² and only cover 18% of the surface area. The {10$\bar{1}$0}, {10$\bar{1}$1}, and {10$\bar{1}$2} facets have surface energies of 141, 149, and 156 meV/Å² and cover considerably 24%, 30%, and 12% of the surface area, respectively. In contrast, {11$\bar{2}$0}, {11$\bar{2}$2}, and {20$\bar{2}$1} all together take ca. 15% of the surface area in hcp Co. The overall surface energy of hcp Co is 146 meV/Å², 10 meV/Å² higher than that of fcc Co.

The fcc Ru has a different morphology as compared with the fcc Co. First, new {221} and {331} facets with a surface energy of 165 and 169 meV/Å² appear with a surface ratio of 6% and 8%, respectively. Along with this, the surface ratios of {100} and {110} facets decrease by 8%. For the {111} and {311} facets, their surface energies are 148 and 183 meV/Å², and the corresponding surface ratios are 61% and 9%, respectively. The overall surface energy of fcc Ru becomes 159 meV/Å². For hcp Ru, the surface ratio of {10$\bar{1}$1} facets with a surface energy of 180 meV/Å² increases significantly up to 41%. This is achieved mainly at the expense of the {0001}, {10$\bar{1}$0}, and {11$\bar{2}$0} facets with surface energies of 163, 181, and 209 meV/Å², respectively. The calculated overall surface energy of hcp Ru is 179 meV/Å², 20 meV/Å² higher than that of fcc Ru.

Changing from 3d Co, 4d Ru to 5d Os, the {100} ratio decreases gradually, and the {110} facets are even diminished. High-index facets, for example, the {322} and {332} facets of fcc Os, increase and together take 29% of the surface area with a surface energy of 190 and 183 meV/Å², respectively. The {111} facets with a surface energy of 168 meV/Å² occupy

dominantly 65% of the surface area. The overall surface energy of fcc Os is 179 meV/Å². The hcp Os has a similar Wulff morphology as hcp Ru. The ratio of {10$\bar{1}$2} with a surface energy of 225 meV/Å² decreases to 10%, whereas the surface ratios of the {0001} and {10$\bar{1}$0} facets increase slightly to 19% and 26% with a surface energy of 182 and 213 meV/Å², respectively. {10$\bar{1}$1} facets with a surface energy of 216 meV/Å² remain the most abundant facets with the surface ratio of 40%. The resulting overall surface energy of hcp Os is 213 meV/Å², 34 meV/Å² higher than that of fcc Os.

We then turn to the TMs of Ni, Rh, Pd, and Ir in Group **II** preferring the fcc phase at ambient conditions. For fcc Ni, the {111} surface energy is slightly lower with a value of 119 meV/Å², as compared with Co, and the corresponding ratio decreases slightly to 56%. The {100} ratio is as high as 20%, which is actually the highest one among the TMs considered. There are considerable {331} facets exposed with a ratio of 12%, which is only about 8% for Ru but zero for the remaining TMs considered. The resulting overall surface energy is 125 meV/Å². As compared with hcp Co, the Ni {10$\bar{1}$1} ratio with a surface energy of 124 meV/Å² increases to 46% at the cost of {10$\bar{1}$2}, {11$\bar{2}$0}, and {11$\bar{2}$2} facets. The {0001} and {10$\bar{1}$0} facets have surface energies of 115 and 121 meV/Å² and occupy 17% and 23% of the surface area, respectively. The resulting overall surface energy of the hcp Ni is 122 meV/Å², 3 meV/Å² lower than that of the fcc Ni.

For fcc Rh, the {111} facets have a surface energy of 125 meV/Å² and cover 65% of the surface area, which is indeed the highest one among the TMs considered. The next populated facets are {100}, and the corresponding surface ratio and surface energy are 17% and 145 meV/Å². The remaining facets exposed are {311}, {221}, and {110} with ratios of 8%, 6%, and 4%, respectively. The calculated overall surface energy is 134 meV/Å². For hcp Rh, the {10$\bar{1}$1} facets have a surface energy of 130 meV/Å², and they are the most populated facets with a ratio of 47%. The next three populated facets are {10$\bar{1}$0}, {0001}, and {11$\bar{2}$2} with ratios of 21%, 17%, and 7%, respectively, and the corresponding surface energies are 129, 122, and 141 meV/Å². The calculated overall surface energy of the hcp Rh is 132 meV/Å², only 2 meV/Å² lower than that of the fcc Rh.

Pd is just on the right side of Rh in the periodic table. Compared to fcc Rh, the ratio of the {111} facets with a surface energy of 83.3 meV/Å² decreases to 51%. The surface ratios of {100}, {221}, and {322} facets remain considerable with ratios of 19%, 10%, and 10%, and the corresponding surface energies are 94.1, 93.1, and 90.8 meV/Å². The remaining 10% of the surface area is populated by, for instance, {211}, {310}, {332}, and {210}. The resulting overall surface energy is 87.4 meV/Å², which is the lowest one among all fcc TMs considered. For hcp Pd, the {10$\bar{1}$1} facets have a surface energy of 87.2 meV/Å² and remain the most populated facets with a surface ratio of 40%. The {10$\bar{1}$0}, {0001}, and {10$\bar{1}$2} facets cover 24%, 18%, and 9% of the surface area, and the corresponding surface energies are 84.6, 77.9, and 93.0 meV/Å². The calculated overall surface energy of the hcp Pd is 85.2 meV/Å², still 2.2 meV/Å² lower than that of the fcc Pd.

The morphology of fcc Ir is close to that of fcc Os, and only {111}, {322}, {332}, and {100} facets are exposed with ratios of 56%, 18%, 14%, and 12%, respectively. The corresponding surface energies are 142, 157, 154, and 175 meV/Å². The resulting overall surface energy is 150 meV/Å². For hcp Ir, the exposed areas are nearly completely occupied by {10$\bar{1}$1},

{10$\bar{1}$0}, and {0001} facets with ratios of 47%, 28%, and 20% (95% in total). The calculated surface energies are 146, 142, and 132 meV/Å², respectively. The resulting overall surface energy is 141 meV/Å². It is 9 meV/Å² lower than that of fcc Ir, and although modest, it still relatively larger than the difference of Pd, Rh, and Ni discussed above.

From the above results, it is clear that the equilibrium morphologies of the fcc TMs are in general truncated octahedron-like shape, and the {111} and {100} facets are preferentially exposed and cover the surface area of 67% at least. The equilibrium morphologies of the hcp TMs are all dihedral-like in shape, and the {0001}, {10$\bar{1}$0}, and {10$\bar{1}$1} facets dominate the surface area of 72% at least. As shown in Figure 4, there remain some changes in the exposed facets and ratios dependent on the composition, which are modest anyhow.

Trend Variation of the Overall Surface Energy and Compensation Effect. To see the trend variation, we plot the calculated overall surface energies for all TMs considered in both the hcp and fcc phases with respect to the experimental cohesive energy in Figure 5a. With gradual increase of the
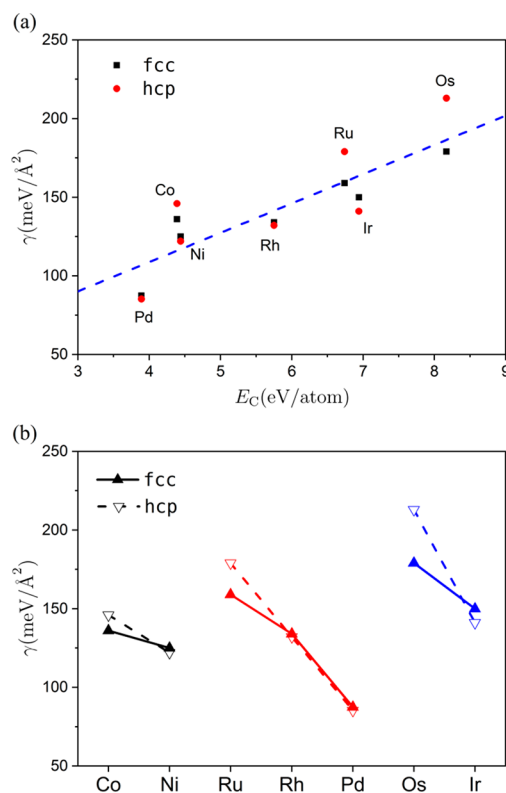

Figure 5. Overall surface energies with respect to the cohesive energy of transition metals (a) and 3d, 4d to 5d transition metals (b) considered.

cohesive energy of Pd, Co, Ni, Rh, Ru, Ir, and Os from 3.89 to 8.17 eV/atom,[69] the corresponding overall surface energies increase proportionally from 85.2 to 213 meV/Å². A good linear correlation is identified: the higher the cohesive energy, the larger the overall surface energy, which is reasonable. The present results are in good agreement with earlier experiments, where the surface tension for many liquid and solid metals was found to depend linearly on the corresponding vaporization or sublimation energy,[84] which correlates directly with the cohesive energy.

We also plot the overall surface energies with respect to the occupation of the valence electrons for the TMs in Figure 5b. Independent of the 3d, 4d, and 5d TMs, the calculated surface energies for both the hcp and fcc phases decrease systematically with an increase of the occupation of d valence electrons. For TMs with more valence electrons occupied and lower-lying d-band center with respect to the Fermi level,[85] the tendency for the orbital hybridization between the TM atoms is weakened, a fact that would lower the energy cost to break the metal−metal bond resulting in a lower surface energy. From Figure 5b, it is interesting to note that for the increase of every valence electron, the decrease in surface energies for 3d hcp and fcc TMs are 24 and 11 meV/Å^2, respectively. For 4d hcp and fcc TMs, the extent of decreases in the surface energies increases considerably to 47 and 36 meV/Å^2 on average, and for 5d hcp and fcc TMs increases further up to 72 and 29 meV/Å^2, respectively. The trend behavior was also in line with previous results, where the surface energies of the TMs show a parabolic dependence on the d occupation and specifically decrease monotonically for the TMs in the right side of the periodic table.[86]

It can be found from Figure 5a that for the TMs in Group I, the fcc surface energies are lower than those of the hcp phase, and the corresponding surface energy differences between fcc and hcp ($\Delta\gamma$(fcc − hcp)) are −10, −20, and −34 meV/Å^2 for Co, Ru, and Os, respectively. However, for the TMs in Group II, the fcc surface energies are higher than those of hcp, and the corresponding $\Delta\gamma$ are 3, 2, 2.2, and 9 meV/Å^2 for Ni, Rh, Pd, and Ir, respectively. The relative order of the surface energy between fcc and hcp is reversed, although the corresponding differences are much smaller. The distinct behavior for the TMs between Group I and II is clearly seen in Figure 6a. Moreover, $\Delta\gamma$ is proportional to E_c: the larger the cohesive energy, the larger the absolute value of the difference, irrespective of the TMs in Group I or II. This is comprehensible since the TMs having a larger cohesive energy implies a stronger metal−metal bond, leading a relative larger surface energy and subsequently the difference between the two phases.

We note that in Figure 1, the bulk energy difference between fcc and hcp ΔE_B is also proportional to the cohesive energy. However, the order between the fcc and hcp phase is completely different with respect to the above surface energy difference as shown in Figure 6a. For the TMs in Group I, fcc bulk energies are higher than those of hcp, but the corresponding surface energies are lower. For the TMs in Group II, the fcc bulk energies are lower than those of hcp, and the corresponding surface energies are higher. This indicates that the higher the bulk energy of a crystal phase, the lower the corresponding surface energy, and the sign of $\Delta\gamma$ is opposite to that of ΔE_B. To better see this, $\Delta\gamma$ is plotted with respect to ΔE_B in Figure 6b. As expected, a perfect linear relationship between $\Delta\gamma$ and ΔE_B is found, and the corresponding slope is negative with a value of −0.18.

To rationalize the result, we note that for the TMs in Group I at ambient conditions, the hcp phase is an energetically more favorable phase with a lower total energy than that of the fcc phase, and a lower total energy indicates a stronger metal−metal bond. As a result, a higher energy cost would be required to create new surfaces by truncating the corresponding metal−metal bond, and the resulting hcp surface energy is higher. Similarly, for the TMs in Group II metals at ambient conditions, the fcc phase is a favorable phase and has a
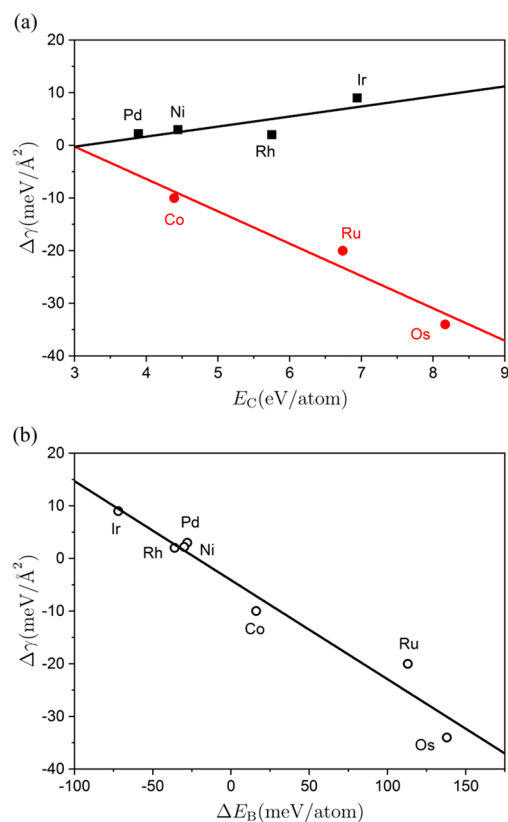

Figure 6. Calculated overall surface difference $\Delta\gamma$ between the fcc and hcp phase with respect to the cohesive energy E_C (a) and the bulk energy difference between the fcc and hcp phase ΔE_B (b).

lower total energy, and the corresponding surface energy would be higher. In other words, for a given TM, the favorable bulk phase with a lower total energy would have a higher surface energy as compensation. The compensation effect rationalizes the opposite sign of $\Delta\gamma$ and ΔE_B as well as their negative slope. Actually, the slope of the measured surface tension with respect to the vaporization energy above-mentioned is about ∼1/6,[84] which is very close to our absolute slope calculated above.

■ DISCUSSION

The compensation effect between the crystal bulk energy and the corresponding surface energy found above would have a great impact on the relative stability of different close-packed phases for the TMs at a small size region particularly in the range of nanometers, where the surface energy plays a significant role in the overall energy. As a matter of fact, the overall energy of nanoparticle per atom, E_{NP}, taking the surface energy contribution into account from the Gibbs−Thomson equation by assuming the particle in a spherical shape with a curvature of radius R,[87−89] could be written as

$$E_{NP} = E_B + \frac{3\Omega\gamma}{R} \tag{4}$$

where Ω is the atomic volume. Concerning the overall energy E_{NP} of a given nanoparticle, the contribution of E_B is constant, but the surface energy term increases rapidly with the decrease of R. For nanoparticles with higher bulk energy, the corresponding surface energy is lower due to the compensation effect. For a given nanoparticle, the corresponding E_{NP} might

become lower than that with a lower bulk energy but a higher surface energy. As a result, by gradual decrease of the particle size to a critical value, the corresponding nanoparticles would transit from a favorable bulk phase to an unfavorable one but with an overall lower total energy, in the case of possible kinetics.

For the TMs of Co, Ru, and Os in Group **I** preferring the hcp bulk at ambient conditions, the above analysis means that the corresponding nanoparticles might transit to the fcc structure at certain small sizes. However, for the TMs of Ni, Rh, Pd, and Ir in Group **II** preferring the fcc bulk at ambient conditions, the corresponding particles might transit to the hcp structure. Since the surface energy differences between the fcc and hcp phases for the TMs in Group **I** are larger than those in Group **II** (Figure 6b), the driving force for the phase transition is stronger and would happen easily.

The above discussions are in good agreement with available experiments. For the three TMs of Co, Ru, and Os in Group **I**, fcc phases have all been found and/or synthesized experimentally. Among other things, fcc Co was one of the most reported ones.[90−97] When Co particles' sizes were larger than 40 nm, hcp Co was the predominant phase with a very small amount of fcc Co, and more fcc Co could be found when the particle size was less than 20 nm.[73] By using Ru precursor containing an optimum ligand and/or another TM as a template, fcc Ru nanoparticles were also synthesized.[25,30,31,75] By adopting similar methods, fcc Os NPs with a size of 1.2 nm were synthesized very recently.[72] In contrast, for the TMs in Group **II**, hcp phases were difficult to form, and so far only few have been reported, in line with the above analysis. Hcp Ni nanoparticles were observed by decreasing the particle size down to 4 nm,[98] and hcp Rh particles were synthesized by solvothermal reaction or electron-beam-induced decomposition of Rh monolayers.[81]

As already indicated above, different crystal phases might be prepared with the help of the optimum ligands by tuning the corresponding surface energies of specific phases and facets.[99] By utilizing the specific template with strong interfacial interaction, a novel crystal phase, such as fcc Ru shell over fcc Pt core, could be achieved as well.[24,100−102] These together with tuning the particle size and strong metal support interaction provide effective ways to control the crystal phase of nanoparticles, which might be useful for designing better catalysts.

CONCLUSION

Based on density functional theory calculations, numerous surfaces of Co, Ru, Os, Ni, Rh, Pd, and Ir in both the fcc and hcp phases are investigated. From the calculated surface energies, equilibrium morphologies are constructed. Irrespective of the transition metals considered, the fcc phase is composed mainly of $\{111\}$ and $\{100\}$ facets, and the hcp phase is composed mainly of $\{10\bar{1}0\}$, $\{10\bar{1}1\}$, and $\{0001\}$ facets. Hcp Co, Ru, and Os with a lower bulk energy have a higher surface energy than the fcc ones, whereas hcp Ni, Rh, Pd, and Ir with a higher bulk energy have a lower surface energy than the fcc ones. A negative linear dependence of the surface energy difference between the fcc and hcp phase on the corresponding bulk energy difference is revealed. The established compensation effect between the bulk energy of a crystal phase and the overall surface energy provides a driving force for the sized-induced phase transition of the support nanoparticles, and the insights revealed might be used to design better catalysts.

AUTHOR INFORMATION

Corresponding Authors

    Wei-Xue Li − *Department of Chemical Physics, School of Chemistry and Materials Science, Hefei National Laboratory for Physical Science at the Microscale, University of Science and Technology of China, Hefei 230026, China;* ◉ orcid.org/ 0000-0002-5043-3088; Email: wxli70@ustc.edu.cn

    Hongjun Fan − *State Key Laboratory of Molecular Reaction Dynamics, Dalian Institute of Chemical Physics, Chinese Academic of Science, Dalian 116023, China;* Email: fanhj@ dicp.ac.cn

Authors

    Hao Lin − *State Key Laboratory of Molecular Reaction Dynamics, Dalian Institute of Chemical Physics, Chinese Academic of Science, Dalian 116023, China; University of Chinese Academic of Sciences, Beijing 100049, China*

    Jin-Xun Liu − *Department of Chemical Engineering and Catalysis Science and Technology Institute, University of Michigan, Ann Arbor, Michigan 48109-2136, United States;* ◉ orcid.org/0000-0002-7499-4197

Complete contact information is available at:
https://pubs.acs.org/10.1021/acs.jpcc.0c02142

Author Contributions

‖These authors contributed equally to this work.

Notes

The authors declare no competing financial interest.

REFERENCES

(1) Greeley, J.; Nørskov, J. K.; Mavrikakis, M. Electronic Structure and Catalysis on Metal Surfaces. *Annu. Rev. Phys. Chem.* **2002**, *53*, 319−348.

(2) Ertl, G.; Knözinger, H.; Weitkamp, J. *Handbook of Heterogeneous Catalysis*; Wiley-VCH Verlag: Weinheim, Germany, 1997.

(3) Xia, Y.; Xiong, Y.; Lim, B.; Skrabalak, S. E. Shape-Controlled Synthesis of Metal Nanocrystals: Simple Chemistry Meets Complex Physics? *Angew. Chem., Int. Ed.* **2009**, *48*, 60−103.

(4) Van Santen, R. A. Complementary Structure Sensitive and Insensitive Catalytic Relationships. *Acc. Chem. Res.* **2009**, *42*, 57−66.

(5) Dahl, S.; Logadottir, A.; Egeberg, R. C.; Larsen, J. H.; Chorkendorff, I.; Törnqvist, E.; Nørskov, J. K. Role of Steps in N_2 Activation on Ru(0001). *Phys. Rev. Lett.* **1999**, *83*, 1814−1817.

(6) Zhang, L.; Roling, L. T.; Wang, X.; Vara, M.; Chi, M.; Liu, J.; Choi, S. I.; Park, J.; Herron, J. A.; Xie, Z.; et al. Platinum-Based Nanocages with Subnanometer-Thick Walls and Well-Defined, Controllable Facets. *Science* **2015**, *349*, 412−416.

(7) Honkala, K.; Hellman, A.; Remediakis, I. N.; Logadottir, A.; Carlsson, A.; Dahl, S.; Christensen, C. H.; Nørskov, J. K. Ammonia Synthesis from First-Principles Calculations. *Science* **2005**, *307*, 555−558.

(8) Behrens, M.; Studt, F.; Kasatkin, I.; Kuehl, S.; Haevecker, M.; Abild-Pedersen, F.; Zander, S.; Girgsdies, F.; Kurr, P.; Kniep, B.-L.; et al. The Active Site of Methanol Synthesis over Cu/ZnO/Al$_2$O$_3$ Industrial Catalysts. *Science* **2012**, *336*, 893−897.

(9) Wang, S.-s.; Jian, M.-z.; Su, H.-y.; Li, W.-x. First-Principles Microkinetic Study of Methanol Synthesis on Cu(221) and ZnCu(221) Surfaces. *Chin. J. Chem. Phys.* **2018**, *31*, 284−290.

(10) Calle-Vallejo, F.; Tymoczko, J.; Colic, V.; Vu, Q. H.; Pohl, M. D.; Morgenstern, K.; Loffreda, D.; Sautet, P.; Schuhmann, W.; Bandarenka, A. S. Finding Optimal Surface Sites on Heterogeneous Catalysts by Counting Nearest Neighbors. *Science* **2015**, *350*, 185−189.

(11) Gao, W.; Zhu, Q.; Ma, D. Nanostructured Catalyst for Fischer−Tropsch Synthesis. *Chin. J. Chem.* **2018**, *36*, 798−808.

(12) Koper, M. T. M. Structure Sensitivity and Nanoscale Effects in Electrocatalysis. *Nanoscale* **2011**, *3*, 2054−2073.

(13) Yu, Y.; Nam, G.-H.; He, Q.; Wu, X.-J.; Zhang, K.; Yang, Z.; Chen, J.; Ma, Q.; Zhao, M.; Liu, Z.; et al. High Phase-Purity 1T′-MoS$_2$- and 1T′-MoSe$_2$-Layered Crystals. *Nat. Chem.* **2018**, *10*, 638−643.

(14) Liang, S.; Teng, F.; Bulgan, G.; Zong, R.; Zhu, Y. Effect of Phase Structure of MnO$_2$ Nanorod Catalyst on the Activity for CO Oxidation. *The. J. Phys. Chem. C* **2008**, *112*, 5307−5315.

(15) Zhang, B.-Y.; Su, H.-Y.; Liu, J.-X.; Li, W.-X. Interplay between Site Activity and Density of BCC Iron for Ammonia Synthesis Based on First-Principles Theory. *ChemCatChem* **2019**, *11*, 1928−1934.

(16) Liu, J.-X.; Li, W.-X. Theoretical Study of Crystal Phase Effect in Heterogeneous Catalysis. *WIREs Comput. Mol. Sci.* **2016**, *6*, 571−583.

(17) Zhao, P.; Cao, Z.; Liu, X.; Ren, P.; Cao, D.-B.; Xiang, H.; Jiao, H.; Yang, Y.; Li, Y.-W.; Wen, X.-D. Morphology and Reactivity Evolution of HCP and FCC Ru Nanoparticles under CO Atmosphere. *ACS Catal.* **2019**, *9*, 2768−2776.

(18) Khodakov, A. Y. Fischer−Tropsch Synthesis: Relations between Structure of Cobalt Catalysts and Their Catalytic Performance. *Catal. Today* **2009**, *144*, 251−257.

(19) Sadeqzadeh, M.; Karaca, H.; Safonova, O.; Fongarland, P.; Chambrey, S.; Roussel, P.; Griboval-Constant, A.; Lacroix, M.; Curulla-Ferré, D.; Luck, F.; et al. Identification of the Active Species in the Working Alumina-Supported Cobalt Catalyst under Various Conditions of Fischer−Tropsch Synthesis. *Catal. Today* **2011**, *164*, 62−67.

(20) Song, D.; Li, J.; Cai, Q. In Situ Diffuse Reflectance FTIR Study of CO Adsorbed on a Cobalt Catalyst Supported by Silica with Different Pore Sizes. *J. Phys. Chem. C* **2007**, *111*, 18970−18979.

(21) Ducreux, O.; Lynch, J.; Rebours, B.; Roy, M.; Chaumette, P. In-Situ Characterisation of Cobalt Based Fischer−Tropsch Catalysts: A New Approach to the Active Phase. *Stud. Surf. Sci. Catal.* **1998**, *119*, 125−130.

(22) Ducreux, O.; Rebours, B.; Lynch, J.; Roy-Auberger, M.; Bazin, D. Microstructure of Supported Cobalt Fischer−Tropsch Catalysts. *Oil Gas Sci. Technol.* **2009**, *64*, 49−62.

(23) Liu, J.-X.; Su, H.-Y.; Sun, D.-P.; Zhang, B.-Y.; Li, W.-X. Crystallographic Dependence of CO Activation on Cobalt Catalysts: HCP Versus FCC. *J. Am. Chem. Soc.* **2013**, *135*, 16284−16287.

(24) Li, W. Z.; Liu, J. X.; Gu, J.; Zhou, W.; Yao, S. Y.; Si, R.; Guo, Y.; Su, H. Y.; Yan, C. H.; Li, W.-X.; et al. Chemical Insights into the Design and Development of Face-Centered Cubic Ruthenium Catalysts for Fischer−Tropsch Synthesis. *J. Am. Chem. Soc.* **2017**, *139*, 2267−2276.

(25) Kusada, K.; Kobayashi, H.; Yamamoto, T.; Matsumura, S.; Sumi, N.; Sato, K.; Nagaoka, K.; Kubota, Y.; Kitagawa, H. Discovery of Face-Centered-Cubic Ruthenium Nanoparticles: Facile Size-Controlled Synthesis Using the Chemical Reduction Method. *J. Am. Chem. Soc.* **2013**, *135*, 5493−5496.

(26) Gu, J.; Guo, Y.; Jiang, Y.-Y.; Zhu, W.; Xu, Y.-S.; Zhao, Z.-Q.; Liu, J.-X.; Li, W.-X.; Jin, C.-H.; Yan, C.-H.; et al. Robust Phase Control through Hetero-Seeded Epitaxial Growth for Face-Centered Cubic Pt@Ru Nanotetrahedrons with Superior Hydrogen Electro-Oxidation Activity. *J. Phys. Chem. C* **2015**, *119*, 17697−17706.

(27) Abo-Hamed, E. K.; Pennycook, T.; Vaynzof, Y.; Toprakcioglu, C.; Koutsioubas, A.; Scherman, O. A. Highly Active Metastable Ruthenium Nanoparticles for Hydrogen Production through the Catalytic Hydrolysis of Ammonia Borane. *Small* **2014**, *10*, 3145−3152.

(28) Ma, H.; Na, C. Isokinetic Temperature and Size-Controlled Activation of Ruthenium-Catalyzed Ammonia Borane Hydrolysis. *ACS Catal.* **2015**, *5*, 1726−1735.

(29) AlYami, N. M.; LaGrow, A. P.; Joya, K. S.; Hwang, J.; Katsiev, K.; Anjum, D. H.; Losovyj, Y.; Sinatra, L.; Kim, J. Y.; Bakr, O. M. Tailoring Ruthenium Exposure to Enhance the Performance of fcc Platinum@Ruthenium Core−shell Electrocatalysts in the Oxygen Evolution Reaction. *Phys. Chem. Chem. Phys.* **2016**, *18*, 16169−16178.

(30) Ye, H.; Wang, Q.; Catalano, M.; Lu, N.; Vermeylen, J.; Kim, M. J.; Liu, Y.; Sun, Y.; Xia, X. Ru Nanoframes with an fcc Structure and Enhanced Catalytic Properties. *Nano Lett.* **2016**, *16*, 2812−2817.

(31) Yao, Y.; He, D. S.; Lin, Y.; Feng, X.; Wang, X.; Yin, P.; Hong, X.; Zhou, G.; Wu, Y.; Li, Y. Modulating fcc and hcp Ruthenium on the Surface of Palladium−Copper Alloy through Tunable Lattice Mismatch. *Angew. Chem.* **2016**, *128*, 5591−5595.

(32) Zhao, M.; Figueroa-Cosme, L.; Elnabawy, A. O.; Vara, M.; Yang, X.; Roling, L. T.; Chi, M.; Mavrikakis, M.; Xia, Y. Synthesis and Characterization of Ru Cubic Nanocages with a Face-Centered Cubic Structure by Templating with Pd Nanocubes. *Nano Lett.* **2016**, *16*, 5310−5317.

(33) Guo, Y.; Azmat, M. U.; Liu, X.; Ren, J.; Wang, Y.; Lu, G. Controllable Synthesis of Hexagonal Close-Packed Nickel Nano-particles under High Nickel Concentration and Its Catalytic Properties. *J. Mater. Sci.* **2011**, *46*, 4606−4613.

(34) Liu, J.-X.; Zhang, B.-Y.; Chen, P.-P.; Su, H.-Y.; Li, W.-X. CO Dissociation on Face-Centered Cubic and Hexagonal Close-Packed Nickel Catalysts: A First-Principles Study. *J. Phys. Chem. C* **2016**, *120*, 24895−24903.

(35) Ashcroft, N.; Mermin, N. *Solid State Physics*; Saunders College: Philadelphia, PA, 1976.

(36) Davies, R. H.; Dinsdale, A. T.; Gisby, J. A.; Robinson, J. A. J.; Martin, S. M. Mtdata - Thermodynamic and Phase Equilibrium Software from the National Physical Laboratory. *CALPHAD: Comput. Coupling Phase Diagrams Thermochem.* **2002**, *26*, 229−271.

(37) Zhao, Z.; Meng, C.; Li, P.; Zhu, W.; Wang, Q.; Ma, Y.; Shen, G.; Bai, L.; He, H.; He, D.; et al. Carbon Coated Face-Centered Cubic Ru−C Nanoalloys. *Nanoscale* **2014**, *6*, 10370−10376.

(38) Guisbiers, G.; Mendoza-Pérez, R.; Bazán-Díaz, L.; Mendoza-Cruz, R.; Velázquez-Salazar, J. J.; José-Yacamán, M. Size and Shape Effects on the Phase Diagrams of Nickel-Based Bimetallic Nanoalloys. *J. Phys. Chem. C* **2017**, *121*, 6930−6939.

(39) Sanchez, J. M.; Stark, J. P.; Moruzzi, V. L. First-Principles Calculation of the Ag-Cu Phase Diagram. *Phys. Rev. B: Condens. Matter Mater. Phys.* **1991**, *44*, 5411−5418.

(40) Gürler, R. A Computer Assessment of the Ru-Rh and Ru-Pd Systems. *J. Alloys Compd.* **1993**, *191*, 31−35.

(41) Dahmani, C. E.; Cadeville, M. C.; Sanchez, J. M.; Morán-López, J. L. Ni-Pt Phase Diagram: Experiment and Theory. *Phys. Rev. Lett.* **1985**, *55*, 1208−1211.

(42) Park, J.; Lee, J. Phase Diagram Reassessment of Ag−Au System Including Size Effect. *CALPHAD: Comput. Coupling Phase Diagrams Thermochem.* **2008**, *32*, 135−141.

(43) Campbell, F. C. *Phase Diagrams: Understanding the Basics*; ASM International: Materials Park, OH, 2012.

(44) Nishizawa, T.; Ishida, K. The Co (Cobalt) System. *Bull. Alloy Phase Diagrams* **1983**, *4*, 387−390.

(45) Lizárraga, R.; Pan, F.; Bergqvist, L.; Holmström, E.; Gercsi, Z.; Vitos, L. First Principles Theory of the hcp-fcc Phase Transition in Cobalt. *Sci. Rep.* **2017**, *7*, 3778.

(46) Quéré, D. Wetting and Roughness. *Annu. Rev. Mater. Res.* **2008**, *38*, 71−99.

(47) Goodman, D. W. Catalytically Active Au on Titania:" yet Another Example of a Strong Metal Support Interaction (SMSI)? *Catal. Lett.* **2005**, *99*, 1−4.

(48) Qi, W. H.; Wang, M. P. Size Effect on the Cohesive Energy of Nanoparticle. *J. Mater. Sci. Lett.* **2002**, *21*, 1743−1745.

(49) Li, S. F.; Zhao, X. J.; Xu, X. S.; Gao, Y. F.; Zhang, Z. Stacking Principle and Magic Sizes of Transition Metal Nanoclusters Based on Generalized Wulff Construction. *Phys. Rev. Lett.* **2013**, *111*, 115501.

(50) Skriver, H. L. Crystal Structure from One-Electron Theory. *Phys. Rev. B: Condens. Matter Mater. Phys.* **1985**, *31*, 1909−1923.

(51) Kresse, G.; Hafner, J. Ab Initio Molecular-Dynamics Simulation of the Liquid-Metal−Amorphous-Semiconductor Transition in Germanium. *Phys. Rev. B: Condens. Matter Mater. Phys.* **1994**, *49*, 14251−14269.

(52) Kresse, G.; Furthmüller, J. Efficient Iterative Schemes for Ab Initio Total-Energy Calculations Using a Plane-Wave Basis Set. *Phys. Rev. B: Condens. Matter Mater. Phys.* **1996**, *54*, 11169−11186.

(53) Kresse, G.; Furthmüller, J. Efficiency of Ab-Initio Total Energy Calculations for Metals and Semiconductors Using a Plane-Wave Basis Set. *Comput. Mater. Sci.* **1996**, *6*, 15−50.

(54) Blöchl, P. E. Projector Augmented-Wave Method. *Phys. Rev. B: Condens. Matter Mater. Phys.* **1994**, *50*, 17953−17979.

(55) Kresse, G.; Joubert, D. From Ultrasoft Pseudopotentials to the Projector Augmented-Wave Method. *Phys. Rev. B: Condens. Matter Mater. Phys.* **1999**, *59*, 1758−1775.

(56) Perdew, J. P.; Burke, K.; Ernzerhof, M. Generalized Gradient Approximation Made Simple. *Phys. Rev. Lett.* **1996**, *77*, 3865−3868.

(57) Perdew, J. P.; Burke, K.; Ernzerhof, M. Generalized Gradient Approximation Made Simple [Phys. Rev. Lett. 77, 3865 (1996)]. *Phys. Rev. Lett.* **1997**, *78*, 1396−1396.

(58) Monkhorst, H. J.; Pack, J. D. Special Points for Brillouin-Zone Integrations. *Phys. Rev. B* **1976**, *13*, 5188−5192.

(59) Davidson, E. R. *Methods in Computational Molecular Physics*; NATO Advanced Study Institute, Series C; Springer: Amsterdam, Netherlands, 1983; p 95.

(60) Gilman, J. J. Direct Measurements of the Surface Energies of Crystals. *J. Appl. Phys.* **1960**, *31*, 2208−2218.

(61) Vitos, L.; Ruban, A. V.; Skriver, H. L.; Kollár, J. The Surface Energy of Metals. *Surf. Sci.* **1998**, *411*, 186−202.

(62) Kumikov, V. K.; Khokonov, K. B. On the Measurement of Surface Free Energy and Surface Tension of Solid Metals. *J. Appl. Phys.* **1983**, *54*, 1346−1350.

(63) Skriver, H. L.; Rosengaard, N. M. Surface Energy and Work Function of Elemental Metals. *Phys. Rev. B: Condens. Matter Mater. Phys.* **1992**, *46*, 7157−7168.

(64) Tran, R.; Xu, Z.; Radhakrishnan, B.; Winston, D.; Sun, W.; Persson, K. A.; Ong, S. P. Surface Energies of Elemental Crystals. *Sci. Data* **2016**, *3*, 160080.

(65) Fiorentini, V.; Methfessel, M. Extracting Convergent Surface Energies from Slab Calculations. *J. Phys.: Condens. Matter* **1996**, *8*, 6525−6529.

(66) Wulff, G. XXV. Zur Frage der Geschwindigkeit des Wachsthums und der Auflösung der Krystallflächen. *Z. Kristallogr. - Cryst. Mater.* **1901**, *34*, 449−530.

(67) Liu, X.; Luo, J.; Zhu, J. Size Effect on the Crystal Structure of Silver Nanowires. *Nano Lett.* **2006**, *6*, 408−412.

(68) Momma, K.; Izumi, F. Vesta 3 for Three-Dimensional Visualization of Crystal, Volumetric and Morphology Data. *J. Appl. Crystallogr.* **2011**, *44*, 1272−1276.

(69) Kittel, C. *Introduction to Solid State Physics*, 8th ed.; Wiley: New York, 2004.

(70) Vincent, F.; Figlarz, M. Quelques précisions sur les paramètres cristallins et l'intensité des raies Debye−Scherrer du cobalt cubique et du cobalt hexagonal. *C. R. Séances Acad. Sci.* **1967**, *264*, 1270−1273.

(71) Urashima, Y.; Wakabayashi, T.; Masaki, T.; Terasaki, Y. Ruthenium, a New Mineral from Horokanai, Hokkaido, Japan. *Mineral. J.* **1974**, *7*, 438−444.

(72) Wakisaka, T.; Kusada, K.; Yamamoto, T.; Toriyama, T.; Matsumura, S.; Ibrahima, G.; Seo, O.; Kim, J.; Hiroi, S.; Sakata, O.; et al. Discovery of Face-Centred Cubic Os Nanoparticles. *Chem. Commun.* **2020**, *56*, 372−374.

(73) Kitakami, O.; Sato, H.; Shimada, Y.; Sato, F.; Tanaka, M. Size Effect on the Crystal Phase of Cobalt Fine Particles. *Phys. Rev. B: Condens. Matter Mater. Phys.* **1997**, *56*, 13849−13854.

(74) Ma, X.; Nolan, A. M.; Zhang, S.; Bai, J.; Xu, W.; Wu, L.; Mo, Y.; Chen, H. Guiding Synthesis of Polymorphs of Materials Using Nanometric Phase Diagrams. *J. Am. Chem. Soc.* **2018**, *140*, 17290−17296.

(75) Joo, S. H.; Park, J. Y.; Renzas, J. R.; Butcher, D. R.; Huang, W.; Somorjai, G. A. Size Effect of Ruthenium Nanoparticles in Catalytic Carbon Monoxide Oxidation. *Nano Lett.* **2010**, *10*, 2709−2713.

(76) Song, C.; Sakata, O.; Kumara, L. S. R.; Kohara, S.; Yang, A.; Kusada, K.; Kobayashi, H.; Kitagawa, H. Size Dependence of Structural Parameters in fcc and hcp Ru Nanoparticles, Revealed by Rietveld Refinement Analysis of High-Energy X-ray Diffraction Data. *Sci. Rep.* **2016**, *6*, 31400.

(77) Owen, E. A.; Yates, E. L. LXVI. X-ray Measurement of the Thermal Expansion of Pure Nickel. *London, Edinburgh, and Dublin Philosophical Magazine and Journal of Science* **1936**, *21*, 809−819.

(78) Hull, A. W. X-ray Crystal Analysis of Thirteen Common Metals. *Phys. Rev.* **1921**, *17*, 571−588.

(79) Tzitzios, V.; Basina, G.; Gjoka, M.; Alexandrakis, V.; Georgakilas, V.; Niarchos, D.; Boukos, N.; Petridis, D. Chemical Synthesis and Characterization of hcp Ni Nanoparticles. *Nanotechnology* **2006**, *17*, 3750−3755.

(80) Schaefer, Z. L.; Weeber, K. M.; Misra, R.; Schiffer, P.; Schaak, R. E. Bridging hcp-Ni and Ni$_3$C via a Ni$_3$C$_{1-X}$ Solid Solution: Tunable Composition and Magnetism in Colloidal Nickel Carbide Nanoparticles. *Chem. Mater.* **2011**, *23*, 2475−2480.

(81) Huang, J. L.; Li, Z.; Duan, H. H.; Cheng, Z. Y.; Li, Y. D.; Zhu, J.; Yu, R. Formation of Hexagonal-Close Packed (HCP) Rhodium as a Size Effect. *J. Am. Chem. Soc.* **2017**, *139*, 575−578.

(82) Chen, L.; Zhang, L.-R.; Yao, L.-Y.; Fang, Y.-H.; He, L.; Wei, G.-F.; Liu, Z.-P. Metal Boride Better Than Pt: HCP Pd$_2$B as a Superactive Hydrogen Evolution Reaction Catalyst. *Energy Environ. Sci.* **2019**, *12*, 3099−3105.

(83) Xiong, Y.; Xia, Y. Shape-Controlled Synthesis of Metal Nanostructures: The Case of Palladium. *Adv. Mater.* **2007**, *19*, 3385−3391.

(84) Overbury, S. H.; Bertrand, P. A.; Somorjai, G. A. Surface Composition of Binary Systems. Prediction of Surface Phase Diagrams of Solid Solutions. *Chem. Rev.* **1975**, *75*, 547−560.

(85) Nørskov, J. K.; Abild-Pedersen, F.; Studt, F.; Bligaard, T. Density Functional Theory in Surface Chemistry and Catalysis. *Proc. Natl. Acad. Sci. U. S. A.* **2011**, *108*, 937−943.

(86) Methfessel, M.; Hennig, D.; Scheffler, M. Trends of the Surface Relaxations, Surface Energies, and Work Functions of the 4d Transition Metals. *Phys. Rev. B: Condens. Matter Mater. Phys.* **1992**, *46*, 4816−4829.

(87) Parker, S. C.; Campbell, C. T. Kinetic Model for Sintering of Supported Metal Particles with Improved Size-Dependent Energetics and Applications to Au on TiO$_2$(110). *Phys. Rev. B: Condens. Matter Mater. Phys.* **2007**, *75*, 035430.

(88) Ouyang, R.; Liu, J.-X.; Li, W.-X. Atomistic Theory of Ostwald Ripening and Disintegration of Supported Metal Particles under Reaction Conditions. *J. Am. Chem. Soc.* **2013**, *135*, 1760−1771.

(89) Yang, C. C.; Li, S. Size-Dependent Phase Stability of Silver Nanocrystals. *J. Phys. Chem. C* **2008**, *112*, 16400−16404.

(90) Cohen-Hyams, T.; Kaplan, W. D.; Yahalom, J. Structure of Electrodeposited Cobalt. *Electrochem. Solid-State Lett.* **2002**, *5*, C75.

(91) Wang, Z. H.; Choi, C. J.; Kim, B. K.; Kim, J. C.; Zhang, Z. D. Characterization and Magnetic Properties of Carbon-Coated Cobalt Nanocapsules Synthesized by the Chemical Vapor-Condensation Process. *Carbon* **2003**, *41*, 1751−1758.

(92) Rong, Y. Phase Transformations and Phase Stability in Nanocrystalline Materials. *Curr. Opin. Solid State Mater. Sci.* **2005**, *9*, 287−295.

(93) Grass, R. N.; Stark, W. J. Gas Phase Synthesis of fcc-Cobalt Nanoparticles. *J. Mater. Chem.* **2006**, *16*, 1825−1830.

(94) Zhang, J.; Lan, C. Q. Nickel and Cobalt Nanoparticles Produced by Laser Ablation of Solids in Organic Solution. *Mater. Lett.* **2008**, *62*, 1521−1524.

(95) Nam, K. M.; Shim, J. H.; Ki, H.; Choi, S.-I.; Lee, G.; Jang, J. K.; Jo, Y.; Jung, M.-H.; Song, H.; Park, J. T. Single-Crystalline Hollow Face-Centered-Cubic Cobalt Nanoparticles from Solid Face-Cen-

tered-Cubic Cobalt Oxide Nanoparticles. *Angew. Chem., Int. Ed.* **2008**, *47*, 9504−9508.

(96) Gnanamani, M. K.; Jacobs, G.; Shafer, W. D.; Davis, B. H. Fischer−Tropsch Synthesis: Activity of Metallic Phases of Cobalt Supported on Silica. *Catal. Today* **2013**, *215*, 13−17.

(97) Nie, L.; Li, Z.; Kuang, T.; Lyu, S.; Liu, S.; Zhang, Y.; Peng, B.; Li, J.; Wang, L. Role of Well-Defined Cobalt Crystal Facets in Fischer−Tropsch Synthesis: A Combination of Experimental and Theoretical Studies. *Chem. Commun.* **2019**, *55*, 10559−10562.

(98) Illy, S.; Tillement, O.; Machizaud, F.; Dubois, J. M.; Massicot, F.; Fort, Y.; Ghanbaja, J. First Direct Evidence of Size-Dependent Structural Transition in Nanosized Nickel Particles. *Philos. Mag. A* **1999**, *79*, 1021−1031.

(99) Sun, Y.; Xia, Y. Shape-Controlled Synthesis of Gold and Silver Nanoparticles. *Science* **2002**, *298*, 2176−2179.

(100) Matthews, J. *Epitaxial Growth*; Elsevier: Cambridge, MA, 2012.

(101) Copel, M.; Reuter, M. C.; Kaxiras, E.; Tromp, R. M. Surfactants in Epitaxial Growth. *Phys. Rev. Lett.* **1989**, *63*, 632−635.

(102) Zhao, M.; Xia, Y., Crystal-Phase and Surface-Structure Engineering of Ruthenium Nanocrystals. *Nat. Rev. Mater.* **2020**. DOI: 10.1038/s41578-020-0183-3.